



Observable Signatures of Stellar-mass Black Holes in Active Galactic Nuclei

Hiromichi Tagawa^{1,2} , Shigeo S. Kimura^{2,3} , Zoltán Haiman^{1,4} , Rosalba Perna^{5,6} , and Imre Bartos⁷ ¹Department of Astronomy, Columbia University, 550 W. 120th Street, New York, NY 10027, USA; ht2613@columbia.edu²Astronomical Institute, Graduate School of Science, Tohoku University, Aoba, Sendai 980-8578, Japan³Frontier Research Institute for Interdisciplinary Sciences, Tohoku University, Sendai 980-8578, Japan⁴Department of Physics, Columbia University, 550 W. 120th Street New York, NY 10027, USA⁵Department of Physics and Astronomy, Stony Brook University, Stony Brook, NY 11794-3800, USA⁶Center for Computational Astrophysics, Flatiron Institute, New York, NY 10010, USA⁷Department of Physics, University of Florida, PO Box 118440, Gainesville, FL 32611, USA

Received 2023 February 8; revised 2023 February 26; accepted 2023 March 3; published 2023 March 21

Abstract

Stellar-mass black holes (BHs) are predicted to be embedded in the disks of active galactic nuclei (AGNs) due to gravitational drag and in situ star formation. However, clear evidence for AGN disk-embedded BHs is currently lacking. Here, as possible electromagnetic signatures of these BHs, we investigate breakout emission from shocks emerging around Blandford–Znajek jets launched from accreting BHs in AGN disks. We assume that most of the highly super-Eddington flow reaches the BH and produces a strong jet, and the jet produces feedback that shuts off accretion and thus leads to episodic flaring. These assumptions, while poorly understood at present, yield observable consequences that can probe the presence of AGN-embedded BHs as well as the accretion process itself. They predict a breakout emission characterized by luminous thermal emission in the X-ray bands and bright broadband nonthermal emission from the infrared to the gamma-ray bands. The flare duration depends on the BH's distance r from the central supermassive BH, varying between 10^3 – 10^6 s for $r \sim 0.01$ – 1 pc. This emission can be discovered by current and future infrared, optical, and X-ray wide-field surveys and monitoring campaigns of nearby AGNs.

Unified Astronomy Thesaurus concepts: Astrophysical black holes (98); Active galactic nuclei (16); Transient sources (1851); Time domain astronomy (2109); High energy astrophysics (739)

1. Introduction

It is a common belief that stars and compact objects (COs), including stellar-mass black holes (BHs), are embedded in the disks of active galactic nuclei (AGNs) due to capture via dynamical interactions between the nuclear star cluster (NSC) and the AGN disk (Ostriker 1983; Syer et al. 1991) and in situ star formation (Levin & Beloborodov 2003; Goodman & Tan 2004; Thompson et al. 2005; Levin 2007). There are several observations supporting this picture. The high metallicity of quasars is presumably related to frequent explosive phenomena of COs and stars in AGN disks (Artymowicz et al. 1993; Wang et al. 2010; Xu et al. 2018; Toyouchi et al. 2022; Wang et al. 2022). The existence of young stars (Genzel et al. 2003; Levin & Beloborodov 2003) and clusters (Milosavljević & Loeb 2004) around Sgr A*, as well as the high metallicity component of NSCs (Antonini et al. 2015; Do et al. 2020; Neumayer et al. 2020; Fahrion et al. 2021), imply that stars, and hence COs, form in situ in AGN disks. Furthermore, the spatial distribution of low-mass X-ray binaries discovered in the Galactic center (Hailey et al. 2018; Mori et al. 2021) is consistent with the evolution of COs and stars in an AGN disk (Tagawa et al. 2020b).

AGN disks are plausible environments for BH–BH (e.g., Bartos et al. 2017; Stone et al. 2017; McKernan et al. 2018; Yang et al. 2019; Tagawa et al. 2020b) and BH–neutron star (NS) mergers (McKernan et al. 2020; Yang et al. 2020; Tagawa et al. 2021b) reported as gravitational-wave (GW) events by the

LIGO (Aasi et al. 2015), Virgo (Acernese et al. 2015), and KAGRA (Akutsu et al. 2021) detectors (Venumadhav et al. 2020; Abbott et al. 2021; The LIGO Scientific Collaboration et al. 2021). This pathway can explain the distributions of masses, mass ratios (Yang et al. 2020; Gayathri et al. 2021), spin vectors (Tagawa et al. 2020a), and correlation between the masses and spin magnitudes (Tagawa et al. 2021a) for the bulk of merging events. Furthermore, AGN disks are promising environments to explain the characteristic properties, high mass (Tagawa et al. 2021b), possible high eccentricity (Romero-Shaw et al. 2020; Samsing et al. 2022; Tagawa et al. 2021c; Gayathri et al. 2022), and hypothesized electromagnetic (EM) counterpart, ZTF19abanrhr (Graham et al. 2020), of the unexpected GW event GW190521 (Abbott et al. 2020). In addition, the first GW event, GW150914 (Abbott et al. 2016), might be associated with a bright gamma-ray event, GW150914-GBM (Connaughton et al. 2016, 2018, but see Greiner et al. 2016; Savchenko et al. 2016; Xiong 2016), which may imply a merger in a gas-rich environment.

Recently, several studies have investigated emission from transients emerging from AGN disks. Zhu et al. (2021c, 2021a), Perna et al. (2021a), Yuan et al. (2022), Wang et al. (2022), and Lazzati et al. (2022) estimated the emission from gamma-ray bursts, and Perna et al. (2021b) and Zhu et al. (2021b) discussed the EM signatures expected from accretion-induced collapse of NSs and white dwarfs. Yang et al. (2022) studied the properties of tidal disruption of stars by stellar-mass BHs, while Grishin et al. (2021) investigated supernova explosions, and Bartos et al. (2017) and Stone et al. (2017) estimated the EM emission produced by thermal radiation and/or outflows from circum-BH disks in AGN disks. There are several studies that investigated possible transients from merging BHs in AGN disks,



Original content from this work may be used under the terms of the [Creative Commons Attribution 4.0 licence](https://creativecommons.org/licenses/by/4.0/). Any further distribution of this work must maintain attribution to the author(s) and the title of the work, journal citation and DOI.

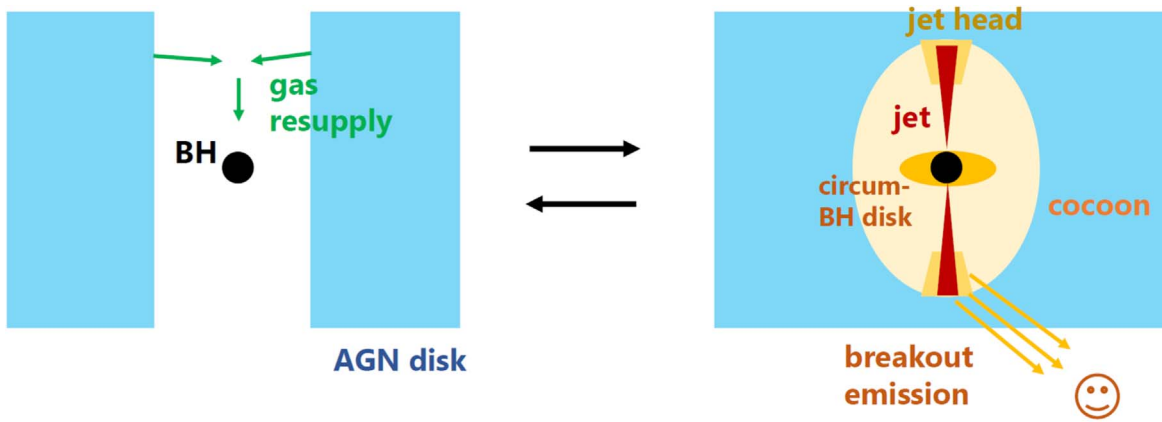


Figure 1. Schematic picture of quiescent phases (left panel) and the breakout emission from the head of a jet launched from a solitary BH (right panel) embedded in an AGN disk.

focusing on the association of the optical flare, ZTF19abanrhr, with the BH merger. McKernan et al. (2019) discussed emission from shocks caused by collision between gas bound to the merged remnant and unbound gas after recoil kicks due to anisotropic radiation of GWs. Graham et al. (2020) assessed the net luminosity and timescales for gas accretion induced by recoil kicks. de Mink & King (2017) considered flares emerging from shocks in a circum-BH disk due to recoil kicks. Kimura et al. (2021a) and Wang et al. (2021a, 2021b), respectively, considered thermal and nonthermal emission from bubbles around BHs due to strong outflows considering continuous and episodic super-Eddington accretion, and Wang et al. (2021a) further considered emission from shocks emerging due to interactions of Blandford–Znajek (BZ) jets (Blandford & Znajek 1977) launched from accreting BHs to the broad line regions. Tagawa et al. (2022, hereafter Paper I) estimated the structure of the cavity created by the BZ jet and dynamical evolution of gas around the BHs. Tagawa et al. (2023, hereafter Paper II) investigated the properties of emission from shocks emerging around jets launched from a BH merger remnant.

In this paper, we apply the method developed in Paper II and evaluate properties and observabilities of thermal and non-thermal emission from shocks emerging around jets launched by accreting solitary BHs due to the BZ effect (Figure 1). We find that thermal emission is bright in X-ray bands, while nonthermal emission is bright in infrared to gamma-ray bands. This emission is predicted to be discoverable by current and future optical and X-ray telescopes, that is, the Zwicky Transient Facility (ZTF), Vera Rubin, XMM-Newton, HiZ-GUNDAM, Einstein Probe, NuSTAR, FORCE, the *Swift* X-ray telescope (XRT), Chandra, JWST, and the Wide-field Infrared Survey Explorer (WISE).

2. Emission

In this section we describe the method for calculating the properties of the breakout emission produced from solitary BHs in AGN disks. More details on this computation are provided in Paper II.

2.1. Mechanisms for Breakout Emission

Here we highlight the physical mechanisms responsible for producing the breakout emission from solitary BHs in AGN disks (see Figure 1 for a schematic representation). In these disks, isolated BHs are surrounded by circum-BH disks since the gas captured by BHs from the AGN disk has enough

angular momentum to circularize around the BHs (Tanigawa et al. 2012). When the circum-BH disk is advection dominated, as expected here, a magnetically dominated state can be realized (e.g., Meier 2001; Kimura et al. 2021b) owing to the accumulation of the magnetic flux in the vicinity of the BH (Cao 2011). Even if the magnetic flux is initially weak, the outflow from the disk converts the toroidal magnetic field generated by the shear motion into a poloidal field (Liska et al. 2020). In these cases, jets from spinning BHs can be launched through the BZ process (Blandford & Znajek 1977). The jet power (L_j) is proportional to the mass accretion rate onto the BH (\dot{m}),

$$L_j = \eta_j \dot{m} c^2, \quad (1)$$

where η_j is the conversion efficiency from rest mass to jet power, which is approximated by $\eta_j \sim a_{\text{BH}}^2$ for a magnetically dominated jet (e.g., Tchekhovskoy et al. 2010; Narayan et al. 2022), a_{BH} is the dimensionless spin of the BH (see Section 2.2 for its choice), and c is the speed of light. Since the power of a shock emerging around the jet and the luminosity of radiation emitted from the shock are roughly proportional to the jet power, the accretion rate onto the BH is a key quantity to determine the observed luminosity from the system.

The accretion rate onto a circum-BH disk in the AGN disk is often evaluated via a modified Bondi–Hoyle–Lyttleton (BHL) rate, as given by Equation (1) of Paper I. To consider a possible reduction from the BHL rate, we parameterized the fraction of the accretion rate onto the BH (\dot{m}) over the BHL rate (\dot{m}_{BHL}) as $f_{\text{acc}} = \dot{m}/\dot{m}_{\text{BHL}}$. For example, low f_{acc} may be predicted due to winds from an accretion disk with a super-Eddington rate although recent simulations suggest that the conversion to wind is moderate (Kitaki et al. 2021) for accretion flows in which the circularization radius (where gas is circularized after being captured by a BH) is much larger than the trapping radius (within which photons are advected to a BH without escaping), as is the case for BHs embedded in an AGN disk. In addition, the accretion rate onto a BH in a cavity during the active phases is estimated to be lower by a factor of a few compared to that without a cavity (Tagawa et al. 2022). As a fiducial value, we simply adopt $f_{\text{acc}} = 1$.

Once the jet collides with the AGN gas, a cocoon of shocked gas forms around the jet. Due to the high pressure of the cocoon, AGN gas around the BH, together with the outer regions of the circum-BH disk, are quickly evacuated. The BH

keeps accreting, and the jet remains active until the inner remnant regions of the truncated circum-BH disk are consumed by the accretion. Subsequently, the BH is quiescent, and the cavity begins to fill in gradually. Finally, AGN gas is recaptured by the BH, and the cocoon reopens a cavity. We predicted in [Paper I](#) that such a cycle repeats many times until the dissipation of the AGN disk.

As the jet collides with unshocked gas in the AGN disk, strong shocks form. During the early phases, photons in the shocked medium cannot escape from the system because they are surrounded by the optically thick AGN disk. As the shock approaches the surface of the AGN disk, thermal photons in the shocks begin escaping from the system, and nonthermal electrons begin to be accelerated due to the formation of collisionless shocks, leading to luminous thermal and nonthermal emission. As nonthermal emission we take into account synchrotron radiation, synchrotron self-Compton (SSC) scattering, and second-order inverse Compton (IC) scattering. Because of the high density of AGN gas, we need to consider synchrotron self-absorption.

In [Paper II](#) we predicted the properties of the breakout emission emerging from merger remnant BHs, and the same formulae can be applied to the emission from solitary BHs. Hence here, by applying the models constructed in [Paper II](#), we discuss the properties and the observability of the breakout emission from solitary BHs.

2.2. Numerical Choices

In the fiducial model we adopt the same parameter values as in [Paper I](#). More specifically, the BH mass is $m = 10 M_{\odot}$; the radial distance of the BH from the central SMBH is $R_{\text{BH}} = 1$ pc; the mass of the SMBH is $M = 10^6 M_{\odot}$; the gas inflow rate from the outer boundary ($R_{\text{out}} = 5$ pc) of the AGN disk is $\dot{M}_{\text{in}} = 1 L_{\text{Edd}}/c^2$, where L_{Edd} is the Eddington luminosity of the SMBH; the angular momentum transfer parameter in the outer AGN disk is $m_{\text{AM}} = 0.15$ (Thompson et al. 2005); the viscous parameter in the inner disk is $\alpha_{\text{AGN}} = 0.1$ (King et al. 2007; Martin et al. 2019); and the opening angle of the injected jet is $\theta_0 = 0.2$ (e.g., Pushkarev et al. 2009; Hada et al. 2013, 2018; Berger 2014).

We set the jet energy conversion efficiency to $\eta_j = 0.1$ considering that spin-up by accretion and spin-down by the BZ jet may be roughly equal at around $a_{\text{BH}} \lesssim 0.3^8$ (e.g., Figure 10 of Narayan et al. (2022)), the fraction of postshock energy carried by the postshock magnetic field and by electrons to $\epsilon_{\text{B}} = 0.03$ (e.g., Panaitescu & Kumar 2001; Uchiyama et al. 2007; Santana et al. 2014) and $\epsilon_{\text{e}} = 0.1$ (e.g., Waxman & Loeb 1999; Panaitescu & Kumar 2001; Sironi et al. 2013; Santana et al. 2014), respectively, and the power-law slope for injected electrons accelerated by the first-order Fermi process to $p = 2.5$.

3. Properties of Breakout Emission

In the following we discuss the properties of the breakout emission (see [Paper II](#) for computational methods).

3.1. Properties of Breakout Emission from Solitary BHs

In the outer regions of $R \gtrsim 0.1$ pc for the fiducial model, since the aspect ratio (H_{AGN}/R) of the AGN disk is large due to intense star formation to stabilize the disk (Thompson et al. 2005), the accretion rates onto BHs, and accordingly the breakout luminosity L_{breakout} , are low (Figure 2(a)). In the inner regions of $R \lesssim 10^{-2}$ pc, L_{breakout} is low since gaps form in these regions, which reduce the accretion rates onto BHs. The accretion rates onto BHs at $R = 1$ and 10^{-2} pc are, respectively, $3 \times 10^{-4} M_{\odot} \text{ yr}^{-1}$ and $3 \times 10^{-3} M_{\odot} \text{ yr}^{-1}$, corresponding to $\sim 10^4$ and 10^5 times the Eddington rate. Despite the fact that the accretion rate and the duration of accretion are, respectively, much lower and longer than for gamma-ray bursts, the range of values for the plasma parameters (ϵ_{e} , ϵ_{B}) can be reasonably adopted from observations of afterglow emission of gamma-ray bursts (e.g., Panaitescu & Kumar 2001; Santana et al. 2014). This is motivated by the consideration that the basic physics of the radiation processes in the two contexts is similar since in both cases the emission is produced by the interaction of a relativistic jet with the surrounding medium. However, we do note that the jet production physics may be different (e.g., Bromberg & Tchekhovskoy 2016; Liu et al. 2017), the compositions of the jets may be different (e.g., Beloborodov 2003; Chen et al. 2023; Kimura et al. 2022), the duration and the accretion rate are different, and the contribution of synchrotron self-absorption to emission is different due to the difference in the density of the ambient material. The above differences may result in significantly different distributions of the plasma parameters between the jets from BHs in AGN disks and those in gamma-ray bursts.

It is predicted that BHs tend to reside in the outer regions with $R \gtrsim 1$ pc since the Type I migration timescale is long, as well as in the inner regions with $R \lesssim 10^{-2}$ pc as annular gaps are predicted to form where migration is slow, causing BHs to accumulate (e.g., Tagawa et al. 2020b; Gilbaum & Stone 2022; Perna et al. 2021b). Therefore, below we consider the two cases with BHs at 1 pc and at 10^{-2} pc as representative examples.

The spectral energy distributions for emission from BHs at $R = 1$ pc and $R = 0.01$ pc in the fiducial model are shown in Figures 3 and 4, respectively. In this model, the thermal emission is computed under the assumption that the radiation energy in the shock is released once the shock becomes optically thin (e.g., Levinson & Nakar 2020). Nonthermal emission is produced from electrons accelerated at collisionless shocks by synchrotron radiation, SSC scattering, and second-order IC scattering.

The nonthermal emission is bright from the infrared to the gamma-ray bands (solid black lines). The three peaks are contributed by synchrotron radiation, SSC scattering, and second-order IC scattering, while the lower cutoff in non-thermal emission is due to synchrotron self-absorption. The thermal emission is mostly bright in X-rays (solid brown lines), and it has a much higher luminosity than the nonthermal emission (due to the reduction by a factor of ϵ_{e} compared to the total energy).

In [Paper I](#) we evaluated the breakout of shocks around a jet produced from a solitary BH and found it to be episodic. Emission phases last for the consumption timescale of the circum-BH disk with $t_{\text{cons}} \sim 300$ yr, followed by quiescent phases lasting for the resupply timescale of $t_{\text{re}} \sim 10^4$ yr at $R \sim 1$ pc, with the cycle repeating. At $R \sim 10^{-2}$ pc, $t_{\text{cons}} \sim 1$ yr and $t_{\text{re}} \sim 10$ yr. By using the duration of emission (solid black

⁸ The spin magnitude of the BHs in the AGN disk is assumed to be lower than that observed for typical X-ray binaries (Reynolds 2021). This is because the former keeps powering a BZ jet while accreting, while the other does not in soft states. The fiducial choice is conservative, and the breakout emission becomes brighter if the spin magnitude is higher.

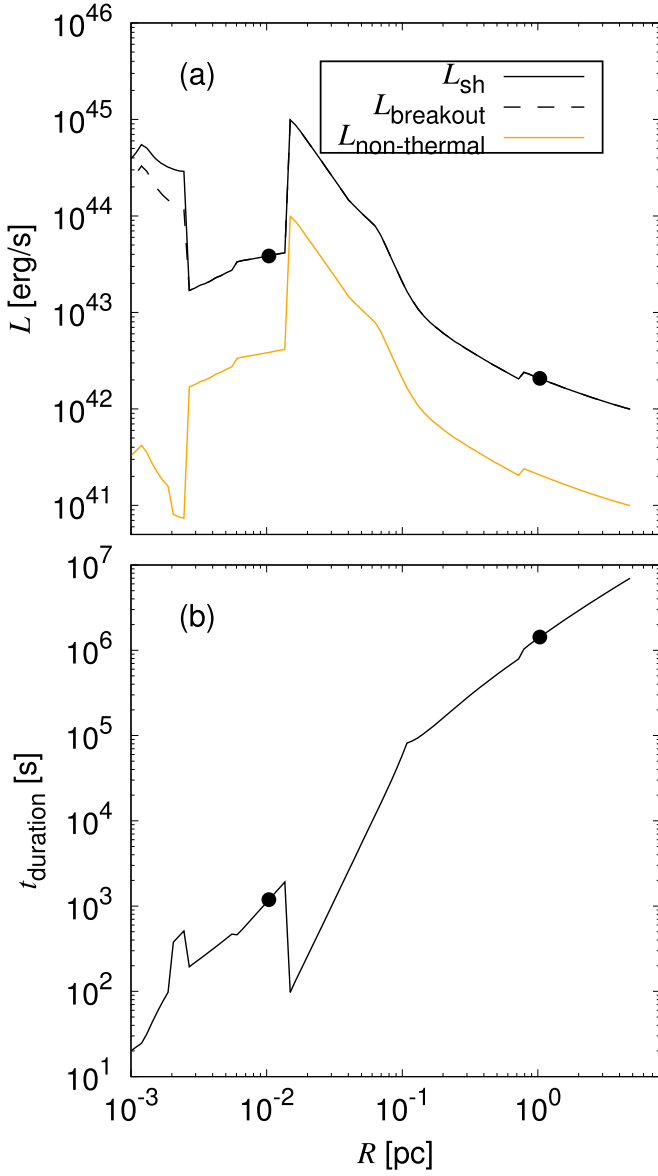


Figure 2. The luminosity and duration as a function of the distance from the SMBH (R) for emission from breakout of shocks produced around solitary BHs in the fiducial model. (a) The shock kinetic (solid black), breakout (dashed black), and non-thermal (solid orange) luminosity. (b) The duration of emission, t_{duration} . The BH locations adopted in the fiducial model are indicated with filled circles superposed on the black solid lines.

line in Figure 2(b)), which is $t_{\text{duration}} \sim 2 \times 10^6$ s at $R \sim \text{pc}$ and ~ 200 s at $R \sim 0.01$ pc, the total duration for breakout emission to be released from one BH over the AGN lifetime time is estimated to be $f_{\text{active}} \sim t_{\text{duration}}/t_{\text{re}} \sim 10^{-5}-10^{-6}$. Here, note that the duration is reduced for the model with $\eta_j = 1$ to 7×10^5 s at $R = 1$ pc and 300 s at $R = 0.01$ pc and enhanced for the model with $f_{\text{acc}} = 0.1$ to 3×10^6 s at $R = 1$ pc and 6×10^3 s at $R = 0.01$ pc. As discussed in Paper I, the number of AGN disk-embedded BHs is $\sim 300 (\dot{M}_{\text{in}}/1 L_{\text{Edd}} c^2)^{1/2}$. Using the predicted mass distribution of $dN_{\text{BH}}/dR \propto R^{-\gamma}$ with $-0.5 \lesssim \gamma \lesssim 0$ (Freitag et al. 2006; Hopman & Alexander 2006; Alexander et al. 2007), we tentatively assume that $N_{\text{BH}} \sim 200$ and ~ 30 BHs are embedded at $R \sim \text{pc}$ and $\sim 10^{-2}$ pc, respectively. Note that these numbers evolve with time and are highly uncertain. With these, the time interval between flares in one AGN is $t_{\text{interval}} \sim t_{\text{re}}/N_{\text{BH}} \sim 50$ yr and

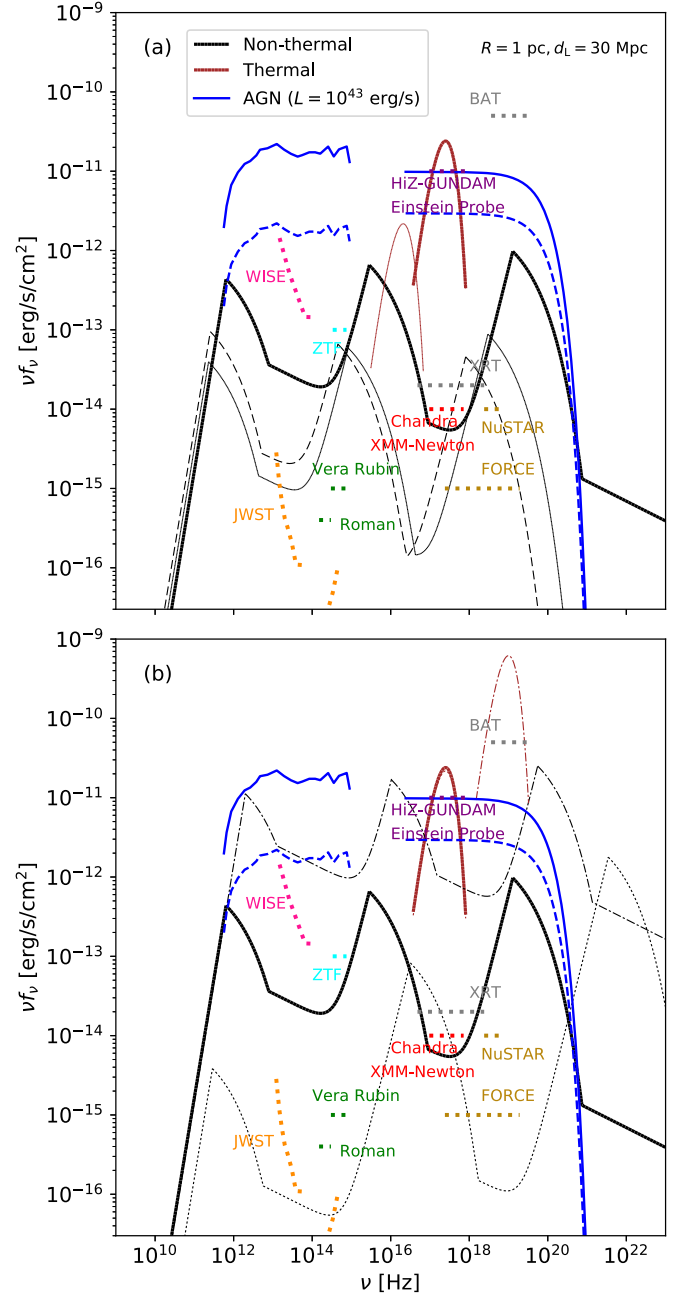


Figure 3. The spectral energy distribution for nonthermal (thick solid black) and thermal (thick solid brown) emission in the fiducial model (Section 2.2) at $R = 1$ pc. The left, middle, and right components in black lines represent synchrotron emission, synchrotron self-Compton (SSC), and second-order inverse Compton (IC) scattering, respectively. Solid and dashed blue lines represent emission from the host AGN and its variability, respectively. Dotted cyan, green, red, purple, gray, gold, pink, and orange lines indicate the sensitivities of ZTF, Vera Rubin and the Roman Space Telescope, Chandra and XMM-Newton, HiZ-GUNDAM and Einstein Probe, the Burst Alert Telescope (BAT) and XRT, NuSTAR and FORCE, WISE, and JWST, respectively. The results are also shown for models with lower accretion rate onto BH ($f_{\text{acc}} = 0.1$, thin solid lines) or lower efficiencies of electron acceleration ($\epsilon_e = 0.01$, thin dashed) in panel (a) or lower magnetic field amplification ($\epsilon_B = 10^{-3}$, thin dotted) or a higher jet efficiency ($\eta_j = 1$, thin dashed-dotted) in panel (b).

~ 0.3 yr at $R \sim \text{pc}$ and $R \sim 10^{-2}$ pc, respectively. From solitary BHs at $R \sim \text{pc}$, thermal emission with luminosity of $\sim 2 \times 10^{42} \text{ erg s}^{-1}$ in X-ray bands (brown line in Figure 3) and nonthermal emission with $\sim 10^{39}-10^{41} \text{ erg s}^{-1}$ in infrared

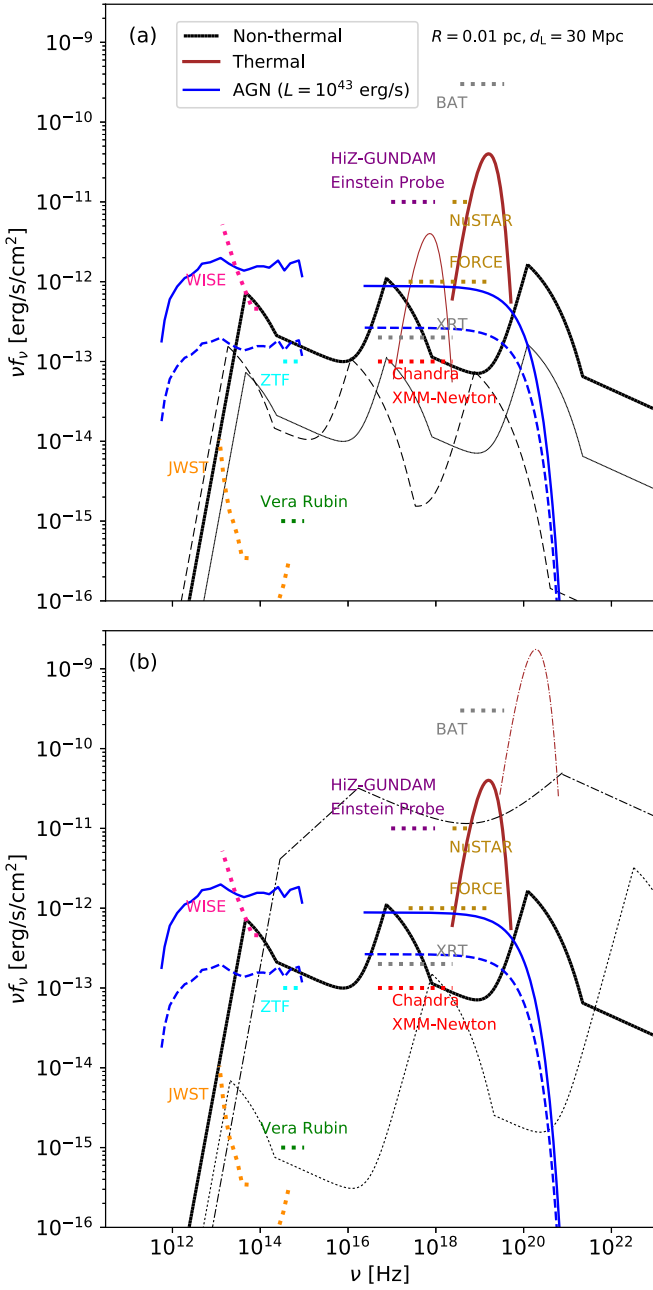


Figure 4. Same as Figure 3 but for BH sources at $R = 0.01$ pc.

to gamma-ray bands (black line in Figure 3) are predicted with duration of $t_{\text{duration}} \sim 0.1$ yr (solid black line in Figure 2(b)) by observing one AGN for $t_{\text{interval}} \sim 50$ yr. From solitary BHs at $R \sim 10^{-2}$ pc, thermal emission with luminosity of $\sim 4 \times 10^{43}$ erg s $^{-1}$ in hard X-ray bands (brown line in Figure 4) and nonthermal emission with luminosity of $\sim 10^{41}$ – 10^{42} erg s $^{-1}$ in optical to gamma-ray bands (black line in Figure 4) are predicted with duration of $\lesssim 10^3$ s by observing an AGN for ~ 0.3 yr.

Here, the luminosity from the host AGN in the relevant energy range is

$$\nu L_{\text{AGN}}(\nu) \sim 10^{42} \text{ erg s}^{-1} (M/10^6 M_{\odot}) (\dot{M}c^2/1 L_{\text{Edd}})(f_{\text{bol}}/10)^{-1}, \quad (2)$$

where f_{bol} is the bolometric correction at the given frequency. As depicted by the blue lines in Figures 3 and 4, we assume

that $f_{\text{bol}} \sim 5$ at $c/\nu = 4400 \text{ \AA}$ and extrapolate the luminosity for $10^{12} \text{ Hz} \lesssim \nu \lesssim 10^{15} \text{ Hz}$ using the cyan or blue points in Figure 7 of Ho (2008) depending on the assumed Eddington rate and $f_{\text{bol}} \sim 10$ in $0.1 \text{ keV} \leq h\nu$ (Ho 2008; Trakhtenbrot et al. 2017; Duras et al. 2020) with the upper exponential cutoff at 300 keV (e.g., Ricci et al. 2018). We also assume that the fraction of the variable luminosity compared to the average luminosity (f_{var}) in optical bands with $t_{\text{duration}} \lesssim 0.1$ yr is $f_{\text{var}} \lesssim 0.1$ (Kozłowski 2016) and that in X-ray bands is $f_{\text{var}} \sim 0.3$ (Soldi et al. 2014; Maughan & Reiprich 2019; dashed blue lines in Figures 3 and 4).

In the optical, X-ray, and gamma-ray bands, the luminosity for nonthermal emission at $R = 0.01$ pc exceeds the variable luminosity (solid black and dashed blue lines in Figure 4). Additionally, the variability of AGNs is typically stronger at shorter wavelengths (Arévalo et al. 2008), while nonthermal emission for $R = 0.01$ pc is brighter at longer wavelengths in the optical bands. This unusual trend can help distinguish the breakout emission from a solitary BH from stochastic AGN variability. Also, the thermal X-ray luminosity clearly exceeds the AGN luminosity at both $R = 1$ pc and 0.01 pc (blue and brown lines in Figures 3 and 4). Hence, nonthermal emission from BHs at $R = 0.01$ pc and thermal emission at $R = 0.01$ pc and $R = 1$ pc can be recognized as unusual variability of AGNs due to their luminosity and color.

However, we do note that the properties of emission are significantly influenced by uncertainties in the model parameters, namely f_{acc} , ϵ_e , ϵ_B , and η_j . Since ϵ_e and ϵ_B are respectively found to vary within the ranges ~ 0.01 – 0.3 and $\sim 10^{-5}$ – 0.1 from GRB afterglow observations (Panaitescu & Kumar 2001; Santana et al. 2014), and η_j can typically range between 0.1 and 1 as discussed above, in Figures 3 and 4 we also show emission models with $\epsilon_e = 0.01$ (thin dashed lines in panel (a)), $\epsilon_B = 10^{-5}$ (thin dotted lines in panel (b)), and $\eta_j = 1$ (thin dashed-dotted lines in panel (b)). Given that f_{acc} is also highly uncertain, we additionally present a model with $f_{\text{acc}} = 0.1$ (thin solid lines in panel (a)) as a representative example. Figures 3 and 4 show that nonthermal emission at $R = 0.01$ pc can be dimmer than the AGN variability if the values of the model parameters are in their lower range. On the other hand, thermal emission is relatively less affected by these parameters. If we assume that η_j is well constrained by numerical simulations (e.g., Narayan et al. 2022), then thermal emission is almost solely influenced by the accretion rate onto the BHs. Thus, by observing the thermal emission, we can improve our understanding of the accretion processes in super-Eddington regimes.

As an additional point in relation to observations, we note that the estimates above suggest that we need to wait a long time to come across breakout emission by monitoring a single AGN. A more viable strategy would be that of observing many AGNs and checking whether there is variability in various bands, as discussed in Section 3.3.

3.2. Differences with Respect to the Emission from Merging Remnants

While the basic physical emission mechanisms are the same for solitary BHs and the post-merger BHs discussed in Paper II, there are some important quantitative differences between the two cases, which we highlight below. (1) Merger remnants tend to be massive compared to isolated BHs. (2) Merger remnants have higher BH spin magnitude, and hence higher conversion

efficiency η_j of mass to jet power. (3) An enhancement of the accretion rate (compared to the solitary BH case) is expected for merger remnants due to shocks emerging in circum-BH disks by GW recoil kicks. (4) The flares from merger remnants are correlated with GW events. Due to (1)–(3), the luminosity of the breakout emission is higher in the case of a post-merger BH, and due to (4) the transients are easier to discover when produced by merger remnants and the associated GW source has already been detected. The above suggests that the emission from solitary BHs is more difficult to observe compared to that from merger remnants; therefore, the search for emission from solitary BHs needs to be strategized, as discussed in the next section.

3.3. Observability of Breakout Emission

Here, we consider whether emission from solitary BHs can be discovered by current and future observing facilities.

The luminosity from nonthermal emission from solitary BHs at $R=0.01$ pc exceeds the sensitivity limit by ZTF, Vera Rubin, XRT, Chandra, XMM-Newton, WISE, and JWST at $d_L=30$ Mpc (solid black, dashed cyan, dashed green, dashed gray, dashed red, dashed pink, and dashed orange lines in Figure 4). Here, the typical variable luminosity of AGNs with duration of $\lesssim 0.1$ yr is (Kozłowski 2016)

$$\nu L_{\text{AGN,vari}}(\nu) \sim 2 \times 10^{40} \text{ erg s}^{-1} (M/10^6 M_\odot) (Mc^2/0.01 L_{\text{Edd}}) (f_{\text{bol}}/5)^{-1} (f_{\text{var}}/0.1), \quad (3)$$

which is generally lower than the luminosity of breakout emission $L_{\text{flare}} \sim f_{\text{acc}} (10^{41} \text{--} 10^{42}) \text{ erg s}^{-1}$, unless the reduction in the accretion rate from the BHL rate is $f_{\text{acc}} \lesssim 0.1$. Additionally, nonthermal emission for $R=0.01$ pc is redder around the optical bands as mentioned in Section 3.1. Thus, we can identify the breakout emission by the magnitude of its luminosity as well as by the color of the flare. Here, note that the luminosity of the breakout emission is roughly proportional to the accretion rate onto the SMBH (e.g., Paper 1). Hence, it reduces the influence of both the AGN accretion rate \dot{M}_{in} and mass M on the detectability of the breakout emission since the AGN luminosity is also proportional to the accretion rate onto the SMBH. However, in pessimistic cases in which the accretion rate onto BHs is lower than assumed in the fiducial model or the efficiencies of electron acceleration or magnetic field amplification are lower, then nonthermal emission is dimmer than the typical variability of AGNs, and hence it would be difficult to observe.

On the other hand, thermal emission from solitary BHs at $R=0.01$ pc and $R=1$ pc can most likely be discovered by several X-ray telescopes (Figures 3 and 4) unless the accretion rate onto BHs is significantly lower than assumed in our fiducial model. For emission from $R=1$ pc, since the flare is as rare as $t_{\text{interval}} \sim 50$ yr per AGN, many ($\sim t_{\text{interval}}/t_{\text{obs}} \sim 50(t_{\text{interval}}/50 \text{ yr})(t_{\text{obs}}/\text{yr})^{-1}$) AGNs need to be simultaneously observed to be discovered within the observational timescale (t_{obs}). This requires wide-field surveys, such as HiZ-GUNDAM/Einstein Probe (Table 1). Multiwavelength observations are likely to be the key to identifying the breakout emission. This is because in the solitary BH model, flares occur simultaneously over a broad range of bands (infrared, optical, and X-ray), while for AGN variability the evolution is delayed depending on the frequency. The actual false-alarm probability for the detection of the breakout emission should be

quantified in future work, using observed multiband AGN light curves.

We also estimate observability when the BH spin magnitude is maximal ($a_{\text{BH}} \sim 1$), and the jet energy conversion efficiency ($\eta_j \sim 1$; Narayan et al. 2022) is maximal as an upper limit (dotted lines in panel (b) of Figures 3 and 4). In this case the luminosity of the breakout emission is enhanced by 1 order of magnitude compared to that in the fiducial model. Additionally, the shock velocity is higher by a factor of ~ 1.6 (Bromberg et al. 2011), and the frequency of the emission is enhanced accordingly. Then, the nonthermal emission from the BH at $R=0.01$ pc would be detectable by ZTF and the HiZ-GUNDAM/Einstein Probe. Additionally, the nonthermal emission for $R=1$ pc can be identified by wide-field surveys in radio bands, such as the Atacama Cosmology Telescope (Naess et al. 2021) and the Large Submillimeter Telescope (Kawabe et al. 2016). Therefore, in this optimistic case, the emission could be easily discovered by several instruments at various wavelengths.

More generally, in the fiducial model nonthermal emission from solitary BHs at $R \sim 10^{-2}$ pc can be discovered by ZTF, Vera Rubin, XRT, Chandra, XMM-Newton, JWST, and WISE as unusually intense and red-colored variability, while thermal emission from solitary BHs at $R \sim 1$ pc can be discovered by HiZ-GUNDAM and Einstein Probe.

4. Conclusions

In this paper we have evaluated the properties of breakout emission from shocks emerging around jets launched from accreting and spinning solitary BHs embedded in AGN disks and discussed the observability of such emission. In our model, accretion, and hence jet formation, are episodic since gas around the BHs is evacuated by the jets; once gas is resupplied, the jet is expected to collide with the gas. Due to the formation of shocks at collision, thermal emission produced by the shocked gas and nonthermal emission produced by accelerated electrons are expected. Our main results are summarized as follows:

1. Thermal and nonthermal emission are bright in X-ray bands and in infrared to gamma-ray bands, respectively.
2. Breakout emission from solitary BHs is harder to observe than from merger remnants because (1) the nonthermal and thermal emission are not as bright and (2) the burst is rare and there is no GW trigger. Hence, catching it requires monitoring a large number of AGNs. However, we can still identify breakout emission from solitary BHs as peculiar flares in nearby AGNs, characterized by broadband nonthermal emission (from the γ -rays to the IR), with superimposed thermal emission and duration that depends on the distance of the BH from the central SMBH, varying between 10^3 and 10^6 s for distances $R \sim 0.01$ – 1 pc.
3. Nonthermal emission from solitary BHs at $R \sim 0.01$ pc from the SMBH with duration of $\sim 10^3$ s can be discovered by infrared, optical, and X-ray telescopes as unusually red-colored variability of less luminous AGNs. Additionally, thermal emission from solitary BHs at $R \sim 1$ pc with duration of $\sim 10^6$ s can be discovered by current and future X-ray telescopes.

We find that the observability of the breakout emission from solitary BHs in AGN disks is strongly influenced by accretion

processes in super-Eddington regimes. To discover signatures from the solitary BHs, the accretion processes and plasma physics should be better understood through numerical simulations. Conversely, if the emission is discovered but their properties are different from what we predict, this would improve our understanding of the underlying accretion processes and plasma physics.

This work was financially supported by Japan Society for the Promotion of Science (JSPS) KAKENHI grant Number JP21J00794 (HT) and 22K14028 (S.S.K.). S.S.K. was supported by the Tohoku Initiative for Fostering Global

Researchers for Interdisciplinary Sciences (TI-FRIS) of MEXT's Strategic Professional Development Program for Young Researchers. Z.H. was supported by NASA grant NNX15AB19G and NSF grants AST-2006176 and AST-1715661. R.P. acknowledges support by NSF award AST-2006839. I.B. acknowledges the support of the Alfred P. Sloan Foundation and NSF grants PHY-1911796 and PHY-2110060.

Appendix Telescopes

We list the name and properties of telescopes in Table 1.

Table 1
The Name and Properties of Telescopes Appropriate for Detecting Electromagnetic Signatures from Solitary BHs in AGN Disks

Telescope Name	Photon Energy	Sensitivity ($\text{erg s}^{-1} \text{cm}^{-2}$)	Field of View (sr)	Operation
JWST	$\sim 0.04\text{--}2$ [eV]	$\sim 10^{-17}\text{--}10^{-15}$ for $t_{\text{int}} \sim 10^4$ s	$\sim 10^{-6}$	pointing telescope
WISE	$\sim 0.05\text{--}0.4$ [eV]	$\sim 10^{-13}\text{--}10^{-12}$ for $t_{\text{int}} \sim 10^4$ s	$\sim 10^{-4}$	pointing telescope
Roman Space Telescope (Spergel et al. 2015)	$\sim 0.6\text{--}1$ [eV]	$\sim 4 \times 10^{-16}$ for $t_{\text{int}} \sim 10^4$ s	~ 0.6	wide-field survey
ZTF (Bellm et al. 2018)	$\sim 1.4\text{--}3.1$ [eV]	$\sim 10^{-13}$ for $t_{\text{int}} \sim 30$ s	0.01	wide-field survey
Vera Rubin (Ivezić et al. 2019)	$\sim 1.2\text{--}3.9$ [eV]	$\sim 10^{-15}$ for $t_{\text{int}} \sim 40$ s	0.003	wide-field survey
Subaru/HSC (Aihara et al. 2018)	$\sim 1\text{--}3$ [eV]	$\sim 10^{-16}\text{--}10^{-15}$ for $t_{\text{int}} \sim 10^3$ s	0.0005	pointing telescope
Tomo-e Gozen (Sako et al. 2018)	$\sim 1.7\text{--}3.4$ [eV]	$\sim 2 \times 10^{-13}$ for $t_{\text{int}} \sim 100$ s	0.006	wide-field survey
Chandra	$\sim 0.2\text{--}10$ [keV]	$\sim 10^{-14}$ for $t_{\text{int}} \sim 2 \times 10^4$ s	6×10^{-5}	pointing telescope
XMM-Newton (Jansen et al. 2001)	$\sim 0.4\text{--}3$ [keV]	$\sim 10^{-14}$ for $t_{\text{int}} \sim 10^4$ s	8×10^{-5}	pointing telescope
HiZ-GUNDAM (Yonetoku et al. 2020)	$\sim 0.4\text{--}4$ [keV]	$\sim 10^{-11}$ for $t_{\text{int}} \sim 10^4$ s	1.2	wide-field survey
Einstein Probe (Yuan et al. 2015)	$\sim 0.5\text{--}4$ [keV]	$\sim 3 \times 10^{-11}$ for $t_{\text{int}} \sim 10^3$ s	1.0	wide-field survey
MAXI (Matsuoka et al. 2009)	$\sim 2\text{--}30$ [keV]	$\sim 7 \times 10^{-11}$ for $t_{\text{int}} \sim 6 \times 10^5$ s	0.07	wide-field survey
NuSTAR (Harrison et al. 2013)	$\sim 10\text{--}30$ [keV]	$\sim 10^{-14}$ for $t_{\text{int}} \sim 10^6$ s	3×10^{-5}	pointing telescope
FORCE (Mori et al. 2016)	$\sim 1\text{--}80$ [keV]	$\sim 10^{-14}(t_{\text{int}}/10^5 \text{ s})^{-1}$	10^{-5}	pointing telescope
Swift X-Ray Telescope (XRT) (Burrows et al. 2005)	$\sim 0.2\text{--}10$ [keV]	$\sim 2 \times 10^{-14}(t_{\text{int}}/10^4 \text{ s})^{-1}$	5×10^{-5}	pointing telescope
Swift BAT (Barthelmy et al. 2005)	$\sim 15\text{--}150$ [keV]	$\sim 10^{-8}(t_{\text{int}}/1 \text{ s})^{-1/2}$	1.4	wide-field survey
Fermi GBM (Meegan et al. 2009)	$\sim 8\text{--}4000$ [keV]	$\sim 10^{-8}\text{--}10^{-6}$ for $t_{\text{int}} \sim 1$ s	$\sim 4\pi$	wide-field survey
INTEGRAL SPI-ACS (Winkler et al. 2003)	$\sim 75\text{--}2000$ [keV]	$\sim 10^{-7}\text{--}10^{-6}$ for $t_{\text{int}} \sim 1$ s	$\sim 4\pi$	wide-field survey

